Inorganic Chemistry

Article

pubs.acs.org/IC

Structural Characterization of Moganite-Type $AlPO_4$ by NMR and Powder X-ray Diffraction

Masami Kanzaki* and Xianyu Xue

Institute for Study of the Earth's Interior, Okayama University, 827 Yamada, Misasa, Tottori 682-0193, Japan

Supporting Information

ABSTRACT: Structural characterization of a new high-pressure $AlPO_4$ phase synthesized at 5 GPa and 1500 °C is reported. The phase is monoclinic ($P2/a$) with a = 8.7437(1) Å, b = 4.8584(1) Å, c = 10.8600(2) Å, β = 90.124(1)° (Z = 6). ^{31}P MAS NMR and two-dimensional (2D) ^{27}Al triple-quantum (3Q) MAS NMR revealed that it contains two tetrahedral P sites of 1:2 abundance ratio, and two tetrahedral Al sites with 1:2 ratio. 2D ^{31}P dipolar-recoupled double-quantum (DQ) MAS NMR and $^{27}Al \rightarrow {}^{31}P$ dipolar-based (through-space) and J coupling-based (through-bond) 3Q-heteronuclear correlation (HETCOR) experiments provided direct information on the linkages of these sites. The crystal structure was solved and refined from synchrotron powder X-ray diffraction data utilizing the information from NMR. The phase is isostructural to moganite, a rare SiO_2 polymorph, and its structure can be derived from the latter via an ordered replacement of tetrahedral Si sites by Al and P. The NMR parameters of the phase were also calculated by first-principles method, which are consistent with those observed. Contrary to the other moganite phases known to date (i.e., SiO_2 and PON), moganite-$AlPO_4$ has a higher-pressure stability field than the corresponding quartz phase. This is the first moganite-type phase found in the ABX_4 system.

INTRODUCTION

$AlPO_4$ is isoelectronic to SiO_2, and the counterparts of several SiO_2 polymorphs, such as quartz, cristobalite, and tridymite, are known at ambient pressure.[1] Because of the difference in ionic radii between Al and P, structural phase transformations different from that of SiO_2 are expected at high pressure. Indeed, a $CrVO_4$-structured phase (space group $Cmcm$) of $AlPO_4$, consisting of octahedral Al and tetrahedral P, has been reported to occur above 7 GPa and 900 °C,[2] but no counterpart in SiO_2 has been experimentally observed to date. Until recently, phase relations in the intermediate pressure region (3−10 GPa) have been poorly studied. Dachille and Roy reported the transition from berlinite (quartz phase) to a new phase at 6 GPa and 500 °C.[3] Seifert reported two high-pressure phases at 6 GPa and 900 °C.[2] However, no further details of these phases were given.

We recently explored the phase relation of the $AlPO_4$ system at 4−10 GPa and 1000−1500 °C through both quench and in situ X-ray diffraction (XRD) experiments. During the course of the study, we found three previously unknown high-pressure phases of $AlPO_4$, and have determined their crystal structures from powder XRD and high-resolution ^{31}P magic-angle spinning (MAS) and ^{27}Al triple-quantum (3Q) MAS nuclear magnetic resonance (NMR) spectroscopic techniques. The crystal structures of two of these phases, an $AlVO_4$-structured ($P\bar{1}$) phase observed at 6 GPa and 1000−1250 °C and a $P2_1/c$ phase observed at 6−7 GPa and 1500 °C, have been reported.[4] The two phases both contain doubly bent chains made of six edge-shared Al polyhedra (including five- and six-coordinated Al), which are joined by PO_4 tetrahedra, and differ only in the packing manner of the chains.[4] These phases have been overlooked by previous in situ diamond anvil cell studies.[5] Neither of them have counterparts in the SiO_2 system. Therefore, all the $AlPO_4$ phases with Al in five-and/or six-coordinated sites, but P in tetrahedral sites do not have counterparts in the AX_2 system. On the other hand, a $CaCl_2$-like phase (in which all cations are in octahedral sites) is known to occur, at even higher pressure for both $AlPO_4$ and SiO_2.[5] Apparently, mixed coordination state for the A cation is unfavored in the AX_2 system.

Here, we report structural characterization of the third new $AlPO_4$ phase that was synthesized at a pressure region (4−5 GPa) between the stability field of berlinite (quartz form) and the two phases described above. The combined techniques of powder XRD, solid-state NMR, and first-principles calculation have been employed. As is shown below, this phase was found to have a moganite-type structure. Moganite is a rare SiO_2 polymorph that has been recognized to have a widespread distribution in microcrystalline silica at the Earth's surface, and is generally regarded to be a metastable phase.[6] No moganite phase previously has been reported in the ABX_4 ($A \neq B$) system. Studies regarding the similarity and dissimilarity of phases between SiO_2 and $AlPO_4$ should provide greater insight into the crystal chemistry of the AX_2 and ABX_4 systems.

EXPERIMENTAL SECTION

Sample Synthesis. High-pressure experiments were conducted using a Kawai-type double-stage multianvil high-pressure apparatus at either the Institute for Study of the Earth's Interior (ISEI) or the beamline BL04B1 of SPring-8. The starting material was reagent-grade $AlPO_4$ (>98% purity) that was dried at 1000 °C for 28 h (the same material as that used in a previous study[4]). It was sealed in a Pt capsule with an outer diameter of 3.0 mm and length of 3.5−4.0 mm. A Cr-doped MgO octahedral pressure cell assembly (with an edge length of 18 mm) was employed. Pressure was estimated from a pressure calibration curve constructed from in situ XRD study with the same

Received: January 24, 2012
Published: May 22, 2012

pressure cell, with an uncertainty of <0.5 GPa. A $W_{97}Re_3$−$W_{75}Re_{25}$ thermocouple with a diameter of 0.2 mm was used to monitor and control temperature with fluctuations of <2 °C. The recovered samples were examined via optical microscopy, and the phases were identified by micro-Raman spectroscopy, ^{31}P and ^{27}Al NMR spectroscopy, and powder XRD. All the data reported hereafter have been obtained on two samples synthesized at 5 GPa and 1500 °C for 1 h, which gave sharp XRD and Raman peaks. Both samples were composed predominantly of the new (moganite-type) $AlPO_4$ phase, with trace amounts of corundum (Al_2O_3) and an unidentified phase.

NMR Spectroscopy. All the NMR spectra have been obtained using a Varian Unity-Inova 400 MHz (9.4 T) spectrometer and a Varian 1.6 mm T3 triple-resonance (HXY) MAS NMR probe at ISEI. The resonance frequencies for ^{31}P and ^{27}Al were 162.1 and 104.3 MHz, respectively. The ^{27}Al chemical shift was referenced to 1 M $Al(NO_3)_3$ aqueous solution. The ^{31}P chemical shift was referenced to 85% H_3PO_4 aqueous solution, using solid $(NH_4)_2HPO_4$ as a secondary standard (1.33 ppm relative to 85% H_3PO_4 at 30 kHz MAS with low-power (~12 kHz) proton decoupling during acquisition). All the chemical shifts were reproducible to better than ±0.1 ppm. The reported NMR spectra have been processed offline with matNMR.[7]

^{31}P MAS NMR spectrum have been acquired at a spinning rate of 30 kHz, a $\pi/4$ pulse of 1.1 μs, and a recycle delay of 8000 s to ensure full relaxation. No decoupling was applied during acquisition. Fifteen transients were averaged. The ^{31}P (and ^{27}Al) spin−lattice relaxation time constant (T_1) values measured with the saturation recovery method can be found in Table 1.

Table 1. ^{31}P and ^{27}Al NMR Results for Moganite-$AlPO_4$ Derived from Experiments and GIPAW Calculations[a]

^{31}P NMR				
P site[b]	δ_i^P(ppm)	fwhm[c](ppm)	relative intensity	T_1 (s)
P1	−27.2	1.55	1	2014(47)
	−28.2			
P2	−24.4	1.51	2.00(0.05)	2036(41)
	−26.4			

^{27}Al NMR						
Al site[b]	F_1 shift (ppm)[d]	δ_i^{Al} (ppm)	C_Q^{Al} (MHz)	η_Q^{Al}	relative intensity	T_1[e] (s)
Al1	45.1	40.1(3)	3.93(2)	0.35(2)	1	46(1)
		39.5	4.36	0.43		
Al2	50.2	44.6(3)	4.02(2)	0.28(2)	2.0(1)	
		42.5	3.33	0.20		

[a]GIPAW calculation results are shown below the observed values. [b]Site numbering corresponds to that for crystallographic sites, and assigned according to relative intensity. [c]Full width at half maximum at a spinning rate of 30 kHz and a magnetic field of 9.4 T. [d]Peak position in the isotropic (F_1) dimension of the 2D 3Q MAS NMR spectrum at a magnetic field of 9.4 T. [e]For both (unresolved) peaks in 1D MAS NMR spectrum.

In order to gain information about spatial proximities among ^{31}P NMR peaks, two-dimensional (2D) ^{31}P dipolar-recoupled double-quantum (DQ)-single quantum (1Q) correlation MAS NMR experiment was also performed. The robust POST-C7 pulse scheme[8] was adopted for DQ excitation/reconversion. In this scheme, the DQ excitation/reconversion period consists of N concatenated POST-C7 elements with each element containing three pulses $(\pi/2)_x(2\pi)_{\bar{x}}(3\pi/2)_x$ and the overall phase of the POST-C7 elements being incremented successively by $2\pi/7$. A series of one-dimensional (1D) experiment at a spinning rate of 10 kHz with the DQ excitation/reconversion period ranging from 200 μs to 1000 μs each (corresponding to 7−35 POST-C7 elements) showed a continuous increase in intensity with increasing DQ excitation/reconversion period. The 2D spectrum has been obtained at a spinning rate of 10 kHz, an excitation/reconversion period of 600 μs each (corresponding to 21 POST-C7 elements), and a recycle delay of 200 s (with one steady-state scan before each acquisition). Four transients were averaged for each of 64 t_1 increments.

^{27}Al MAS NMR spectrum has been acquired with a spectral width of 2 MHz, a pulse of 0.5 μs (~30° tip angle for selective central transition), a recycle delay time of 3 s, and a spinning rate of 30 kHz. A small background signal from the probe/rotor (as measured on the empty rotor) has been subtracted from the reported spectrum. Linear prediction has been applied to remove the rolling baseline resulting from spectrometer deadtime (ca. 8 μs).

Because ^{27}Al MAS NMR spectra are often broadened by second-order quadrupolar coupling, high-resolution 2D ^{27}Al triple-quantum (3Q) MAS NMR spectra were also obtained using the three-pulse z-filter sequence.[9] The optimized lengths (with a radio frequency (RF) field of 208 kHz) for the 3Q excitation and 3Q → 0Q reconversion pulses were 2 and 0.7 μs, respectively, and the length of the third soft z-filter $\pi/2$ pulse was 11 μs. A delay of 20 μs was kept between the last two pulses. Eighty rotor-synchronized t_1 increments (33 μs) were acquired at a spinning rate of 30 kHz and a recycle delay time of 60 s (with one steady-state scan before each acquisition). Twenty-four scans were averaged for each. Shearing and chemical shift reference in the isotropic (F_1) dimension follows the convention of Amoureux and Fernandez.[10]

The peak shapes of the MAS cross sections of the 2D 3Q MAS NMR spectrum have been simulated iteratively offline with matNMR,[7] and that of the 1D MAS NMR spectrum was calculated with the STARS software (Varian, Inc.), using the same relative intensity, chemical shift, and quadrupolar coupling parameters derived from 3Q MAS NMR, and taking into consideration of all the $\pm m$ to $\pm(m-1)$ transitions ($m = {}^1/_2, {}^3/_2$, and ${}^5/_2$), as well as the finite probe bandwidth (ca. 0.6 MHz).

In order to assist phase identifications/peak assignment, high-resolution 2D ^{27}Al → ^{31}P 3Q-HETCOR experiments that correlate the high-resolution ^{27}Al isotropic spectrum free from second-order quadrupolar broadening with ^{31}P MAS spectrum were also carried out. Both through-space 3Q-HETCOR experiment utilizing dipolar interactions for polarization transfer (denoted 3Q-D-HETCOR) and through-bond 3Q-HETCOR experiment utilizing scalar J-coupling for polarization transfer (denoted 3Q-J-HETCOR) have been performed using the SPAM-3Q-D-HETCOR and SPAM-3Q-J-HETCOR sequences.[11] For both experiments, the sequence starts with an initial strong pulse of 3Q excitation (with an RF field at ~190 kHz and an optimized length of 2.2 μs), two pulses (including a strong pulse with an RF field at ~190 kHz and an optimized length of 0.8 μs and a weak SPAM (soft pulse added mixing) pulse with an optimized length of 13 or 15 μs) with a minimal time interval in between for 3Q to −1Q conversion on the ^{27}Al channel. The gain in signal intensity has been found to be a factor of ~2, compared to the corresponding sequence without the SPAM scheme, similar to that reported previously.[11] Chemical shift reference in the ^{27}Al isotropic (F_1) dimension is the same as that of ^{27}Al 3Q MAS NMR described above.

For the ^{27}Al → ^{31}P 3Q-D-HETCOR experiment, polarization transfer from ^{27}Al to ^{31}P was achieved by a pair of cross-polarization (CP) contact pulses on both channels. A relatively low power (ca. 14 kHz) on the ^{27}Al channel during CP was used to improve the spin-lock efficiency of the quadrupolar ^{27}Al. A ramped power (with a width of ca. 10 kHz) on the ^{31}P channel was used to improve the stability of CP. A contact time of 8 ms has been used for the 2D spectrum. A phase cycle of 48, including a 12-step phase cycle in 30° step for the first pulse while keeping the phases of the second and third pulses zero to select the 0 → 3Q → 0Q, ±1Q → −1Q pathway, and a 2-step cycle each for the ^{27}Al and ^{31}P contact pulses during CP, similar to that described in Wiench et al.[11] was used. No decoupling was applied during acquisition. Eighty rotor-synchronized t_1 increments (33 μs) were acquired at a spinning rate of 30 kHz and a recycle delay time of 30 s (with one steady-state scan before each FID). Forty-eight transients were averaged for each.

For the ^{27}Al → ^{31}P 3Q-J-HETCOR experiment, polarization transfer from ^{27}Al to ^{31}P was achieved by refocused INEPT. Following a $\pi/2$ pulse on the ^{27}Al channel (that purges the signal for hyper-

dx.doi.org/10.1021/ic300167k | Inorg. Chem. 2012, 51, 6164−6172

complex treatment), the ^{27}Al magnetization evolves under ^{27}Al–^{31}P heteronuclear J-coupling during the first spin–echo ($2\tau_1$) period. Simultaneous $\pi/2$ pulses on both channels then convert the ^{27}Al antiphase coherence (with respect to J-coupled ^{31}P) into antiphase ^{31}P coherence. The latter evolves under ^{27}Al–^{31}P heteronuclear J-coupling into an in-phase signal at the end of the second spin–echo ($2\tau_2$) period before detection on the ^{31}P channel. The RF power for both ^{27}Al and ^{31}P pulses during the refocused INEPT were adjusted to yield a $\pi/2$ pulse length (selective central transition for ^{27}Al) of 15 μs. A phase cycle of 48, including a 12-step phase cycle in 30° step for the first pulse as described above, and a 2-step cycle each for the simultaneous polarization-transfer ^{27}Al and ^{31}P $\pi/2$ pulses, similar to that of Wiench et al.[11] was used. No decoupling was applied during acquisition. In preliminary 1D experiments with a series of rotor-synchronized τ_1 and τ_2 times (1 to 40 ms), maximal intensity for both peaks occurs near 2–3 ms for both τ_1 and τ_2. The 2D experiment has been performed at a spinning rate of 30 kHz with a rotor-synchronized τ_1 of 2 ms and τ_2 of 3 ms. Thirty-two rotor-synchronized t_1 increments (100 μs) were acquired at a spinning rate of 30 kHz and a recycle delay time of 60 s (with one steady-state scan before each acquisition). Forty-eight transients were averaged for each.

The States–Haberkorn–Ruben (hypercomplex) method has been used to achieve quadrature detection in t_1 for all the 2D experiments.

First-Principles Calculations. First-principles calculations of NMR properties for crystalline solids have become increasingly routine and reliable.[12] We have performed first-principles density functional theory (DFT) calculations for structural optimization and NMR parameters in order to confirm the crystal structure determined from powder XRD and the assignment of NMR peaks for moganite $AlPO_4$. Berlinite was also calculated and used as a secondary chemical shift reference for ^{27}Al and ^{31}P. The calculation was conducted using the Quantum-ESPRESSO (QE) package.[13]

First, the crystal structure obtained from XRD data was relaxed using the PWscf code of the QE package. Ultrasoft pseudopotentials (Al.pbe-n-van.UPF, P.pbe-n-van_ak.UPF, and O.pbe-van_ak.UPF from http://www.quantum-espresso.org) with a GGA functional proposed by Perdew, Burke, and Ernzerhof[14] were adopted. The kinetic energy cutoff was 50 Ry.

NMR chemical shielding and electric field gradient tensors were then calculated on the relaxed structure using the gauge including projector augmented wave (GIPAW) method[15] implemented in QE. Self-consistent field (scf) calculation was made using the PWscf code with pseudopotentials suitable for GIPAW. Chemical shielding and electric field gradient tensors were calculated using the GIPAW code in the QE package. These pseudopotentials (for Al, P, and O atoms) were produced using a pseudopotential generation program (ld1) available in the QE package. For Al and P, 3s and 3p orbitals were treated as valence states; for oxygen, 2s and 2p orbitals were treated as valence states. Norm-conserving Troullier-Martins pseudopotentials[16] with two projectors for each angular-momentum channel were used. The kinetic energy cutoff for the scf calculation was 100 Ry. For all the calculations, the Brillouin zone was sampled with the Monkhorst-Pack scheme using a 4 × 4 × 2 and 4 × 4 × 6 grids for the berlinite and moganite phases, respectively.

The ^{31}P and ^{27}Al isotropic chemical shifts (δ_i^P and δ_i^{Al}) of moganite were calculated by setting the corresponding values of berlinite to those experimentally observed (−24.7 and 42.7 ppm, respectively[17,18]). For the calculation of ^{27}Al quadrupolar coupling constant (C_Q^{Al}), a nuclear quadrupole moment of 146.6 mb was used.[19] Similar GIPAW calculations for $AlPO_4$ phases with open framework structures have predicted ^{27}Al and ^{31}P chemical shifts within a few ppm of the observed values.[20,21]

Powder X-ray Diffraction. For phase identification and initial structural analysis, powder XRD data were obtained using a SmartLab diffractometer (Rigaku Co.) operated at 40 kV and 30 mA. It has a Bragg–Brentano configuration with a Cu target and a 1D detector (D/TeX Ultra). An incident monochromator was present to select Cu Kα_1 radiation. For structural refinement by the Rietveld method, the synchrotron powder XRD pattern was obtained at the beamline BL19B2 of SPring-8. A large Debye–Scherrer camera with an imaging plate detector was used.[22] The measurement procedure is identical to that of our previous study.[4] The powdered sample was loaded into a borosilicate glass capillary with a 0.3-mm outer diameter. The exposure time was 10 min. The wavelength of the X-ray beam used was 0.500291 Å, calibrated using the NIST-certified CeO_2 reference material (SRM 674b) by measuring under the same condition except for shorter exposure time (5 min). The glass capillary resulted in complex background at low angles. In order to better fit the background intensity arising from the capillary for the Rietveld refinement, an empty capillary was also measured.

The crystal structure of the phase was initially solved using the ab initio structural determination program FOX,[23] which employs a real-space searching with parallel tempering optimization algorithm. As reported for other high-pressure $AlPO_4$ phases in our previous study,[4] information regarding the numbers of unique P and Al sites, and the oxygen coordination number around P obtained from NMR were utilized for the FOX calculations.

The structure obtained with FOX was further refined with the Rietveld technique using the RIETAN-FP program.[24] For the profile function, the pseudo-Voigt function was adopted. Because of the coexistence of trace other phases in the samples, corundum (also observed by NMR) and platinum (from the capsule) were also included for the Rietveld refinement. For these trace phases, only the scale factors and lattice parameters were refined. There are also several small peaks that cannot be indexed with any known phases. These peaks are likely due to trace amount of an unknown phase, which is also revealed by NMR. The crystal structure has been drawn by VESTA.[25]

RESULTS AND DISCUSSION

^{31}P MAS and DQ-1Q Correlation MAS NMR. The ^{31}P MAS NMR spectrum for a sample synthesized at 5 GPa and 1500 °C contains two main peaks near −27.2 and −24.4 ppm with an integrated intensity ratio of 1:2, and a very weak broader peak at a more-negative chemical shift (see Figure 1 and Table 1). The ^{31}P T_1 of the former two are similar (~2000 s), whereas that of the minor peak is much shorter (more prominent at shorter recycle delay), suggesting that the latter is most likely due to a minor impurity phase. The similarity in T_1, coupled with the long recycle delay time (8000 s after a $\pi/4$ pulse) employed, ensure that the relative integrated intensity of the two main peaks faithfully reflects their abundance ratio (1:2). The chemical shifts are close to (but not identical to) that of the ambient-pressure $AlPO_4$ polymorph, berlinite (−24.7 ppm[17]), falling into the range known for tetrahedral P.[33] The DFT-calculated isotropic chemical shifts for the two P

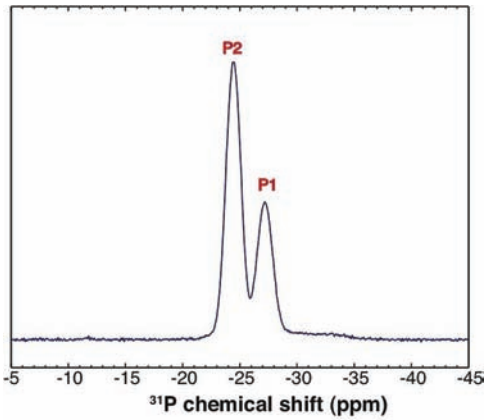

Figure 1. ^{31}P MAS NMR spectrum of moganite-$AlPO_4$. The weak broad intensity at less than −30 ppm is attributable to minor coexisting phosphate phase.

dx.doi.org/10.1021/ic300167k | Inorg. Chem. 2012, 51, 6164–6172

sites are also compared in Table 1, which are generally consistent with those observed (within 2 ppm for the chemical shifts, and within 1 ppm for the peak separation between the two sites).

A 2D ^{31}P dipolar-recoupled DQ-1Q correlation MAS NMR spectrum acquired with the POST-C7 sequence[8] at a spinning rate of 10 kHz with an excitation/reconversion period of 600 μs each is shown in Figure 2. It contains four peaks: two diagonal

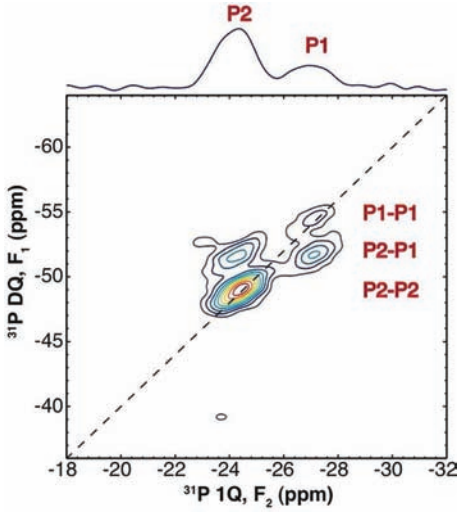

Figure 2. Rotor-synchronized ^{31}P dipolar-recoupling DQ-1Q correlation MAS NMR spectrum acquired using the POST-C7 pulse scheme[8] with total projection along F_2 for moganite-$AlPO_4$. A Gaussian line broadening of 100 Hz has been applied to both dimensions. The contours have been plotted in a linear intensity scale from 10% to 100% of the maximum intensity in increments of 10%. The dashed line is a guide for the positions of diagonal peaks.

peaks corresponding to the two ^{31}P (1Q) MAS NMR peaks at −27.2 and −24.4 ppm, and a pair of cross peaks between the two. This clearly indicates that the two ^{31}P peaks near −27.2 and −24.4 ppm belong to a single phase (the dominant $AlPO_4$ phase).

Therefore, the quantitative 1D ^{31}P MAS NMR and 2D DQ-1Q correlation MAS NMR together suggest that the sample consists dominantly of an $AlPO_4$ phase with two tetrahedral P sites of 1:2 abundance ratio.

^{27}Al MAS and 3Q MAS NMR. The ^{27}Al MAS NMR spectrum of the sample contains (partially) overlapping MAS patterns from second-order quadrupolar coupling (Figure 3). In order to better resolve the different components, 2D rotor-synchronized ^{27}Al 3Q MAS NMR spectra have been obtained at a spinning rate of 30 kHz (Figure 4). The spectrum contains two peaks in the isotropic dimension near 45.1 and 50.2 ppm, with an integrated intensity ratio of 1:2 (see Figure 4a). The MAS cross sections of both peaks can each be well-simulated by a single typical MAS pattern (see Figure 4b). The obtained results for the ^{27}Al isotropic chemical shift (δ_i^{Al}), quadrupolar coupling constant (C_Q^{Al}) and electric field gradient asymmetry parameter (η_Q^{Al}) are tabulated in Table 1. The DFT-calculated NMR parameters for the two Al sites are also shown in Table 1. All the calculated parameters are in reasonable agreement with the experimental results (within ~2 ppm, 0.7 MHz and 0.08 for δ_i^{Al}, C_Q^{Al}, and η_Q^{Al}, respectively). The NMR parameters for the two Al sites are overall similar, differing in δ_i^{Al} by 4.5 ppm, and in C_Q^{Al} by ~0.1 MHz. The δ_i^{Al} values for both peaks (40.1, 44.6

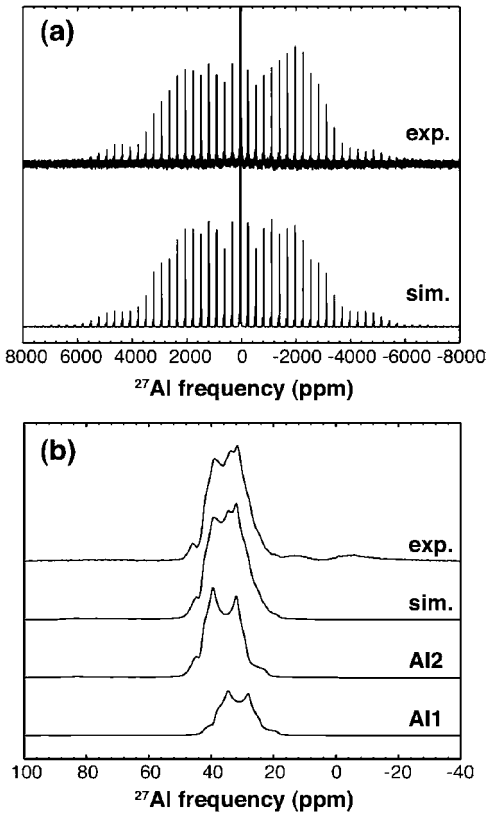

Figure 3. ^{27}Al MAS NMR spectra ((a) entire frequency range and (b) central band) of moganite-$AlPO_4$. Also shown below the experimental spectra are the simulated spectra and the two Al sites of 2:1 abundance ratio obtained using parameters reported in Table 1.

ppm) are similar to that of $AlPO_4$ berlinite (42.7 ppm[18]), and well within the known range for tetrahedrally coordinated Al.[26] Although it is known that the 3Q MAS NMR experiment generally may not be quantitative, with the efficiencies for 3Q coherence excitation and its subsequent conversion to 0Q or 1Q (and thus the relative intensities) varying with C_Q,[27] the similarity in C_Q suggests that the integrated intensity ratio may be reasonably taken to represent their true population ratio. Furthermore, using the same parameters for the two Al sites with 1:2 abundance ratio, both the spinning sideband intensity pattern and central band peak shape of the 1D ^{27}Al MAS NMR spectrum can be reasonably reproduced (Figure 3). As confirmed by 2D ^{27}Al−^{31}P 3Q-HETCOR experiments described below, the two ^{27}Al isotropic peaks belong to the same phase as the two ^{31}P MAS peaks described above. Together this suggests that the $AlPO_4$ phase has two tetrahedral P sites of 1:2 abundance ratio, as well as two tetrahedral Al sites of 1:2 abundance ratio.

There are also two very weak peaks near 12 ppm and −9 ppm in the 1D ^{27}Al MAS NMR spectrum that cannot be attributed to the dominant $AlPO_4$ phase (Figure 3b). These two peaks are also present in the 2D ^{27}Al 3Q MAS NMR spectrum at F_1 positions near 20 and 9 ppm, respectively (outside the frequency range shown in Figure 4). The former peak is also ubiquitously present in other samples synthesized from the same starting material at 5−7 GPa and 1000−1500 °C, and is attributable to minor Al_2O_3 corundum.[4] The latter is consistent with octahedral Al and could correspond to the weak additional ^{31}P MAS NMR peak shown in Figure 1, suggesting the trace presence of an additional aluminophosphate phase.

dx.doi.org/10.1021/ic300167k | Inorg. Chem. 2012, 51, 6164−6172

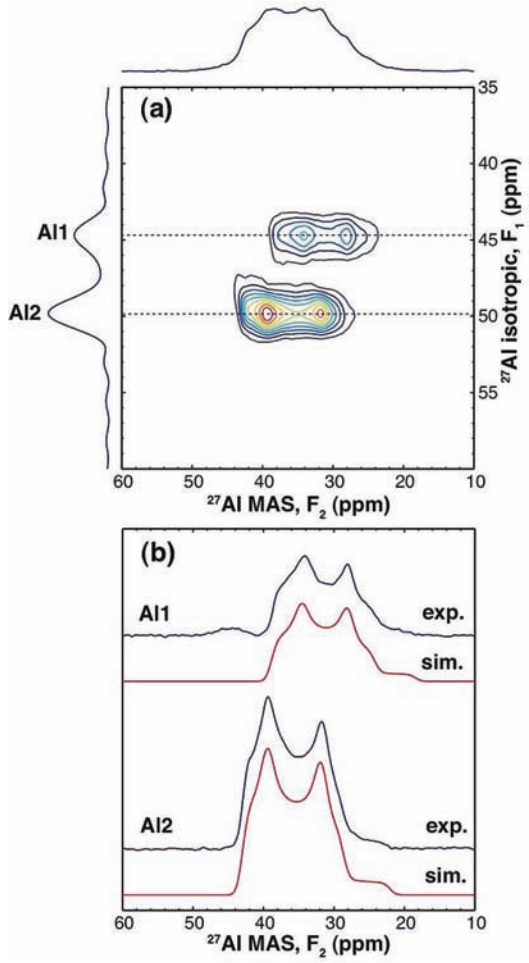

Figure 4. (a) Rotor-synchronized ^{27}Al 3Q MAS NMR spectra with total projections along both dimensions for moganite-$AlPO_4$. A Gaussian line broadening of 50 Hz has been applied to both dimensions. The contours have been plotted in a linear intensity scale from 10% to 100% of the maximum intensity in increments of 10%. (b) MAS cross sections for the two Al sites (at positions indicated by dashed lines in panel a) and the respective simulated spectra underneath as labeled.

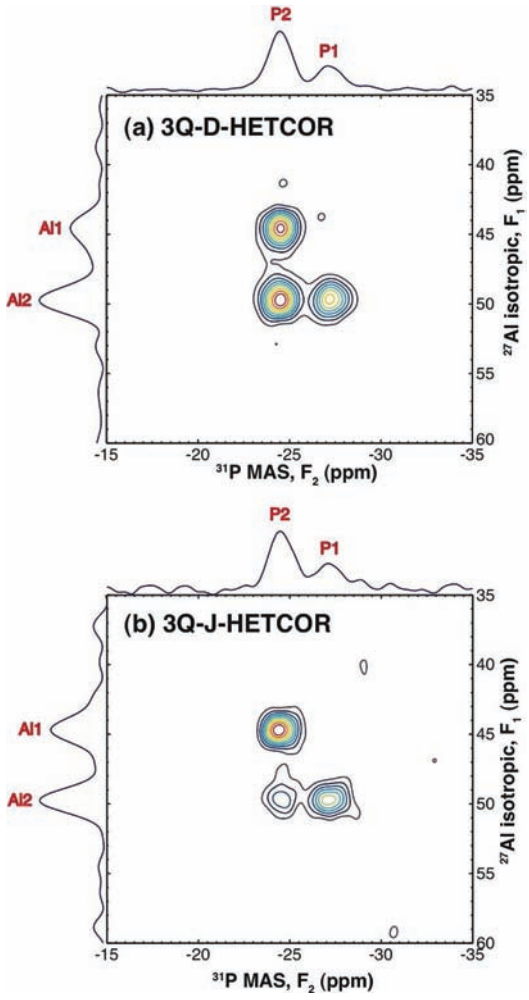

Figure 5. Rotor-synchronized (a) ^{27}Al → ^{31}P 3Q-D-HETCOR spectra and (b) 3Q-J-HETCOR spectra, with total projections along both dimensions for moganite-$AlPO_4$. A Gaussian line broadening of 100 Hz has been applied to both dimensions. The contours have been plotted in a linear intensity scale from 10% to 100% of the maximum intensity in increments of 10%.

^{27}Al → ^{31}P 3Q-D-HETCOR and 3Q-J-HETCOR spectra. High-resolution 2D (dipolar) ^{27}Al → ^{31}P 3Q-D-HETCOR have been obtained at a spinning rate of 30 kHz and a contact time of 8 ms (see Figure 5a). The spectrum contains three cross peaks (P1−Al2, P2−Al1, P2−Al2) with almost equal intensity. The observation of cross peaks between the two Al peaks with one or both of the two P peaks (that have been confirmed to belong to the same phase by ^{31}P DQ-1Q correlation NMR) suggests that all these sites belong to the same $AlPO_4$ phase. As the intensity is related to the number and distances of P(Al) around each Al (P), it may be inferred that Al1 (P1) are linked only to P2 (Al2) (via oxygens), and Al2 (P2) are linked to equal numbers of P1 (Al1) and P2 (Al2) (via oxygens). The lack of Al1−P1 cross peak suggests the absence of Al1−O−P1 linkages. As is clear after the crystal structure analysis from XRD, this configuration is completely in accord with the determined crystal structure.

High-resolution 2D (J coupling-based) ^{27}Al → ^{31}P 3Q-J-HETCOR spectrum of the $AlPO_4$ sample is shown in Figure 5b. The spectrum similarly contains three cross peaks (P1−Al2, P2−Al1, P2−Al2). Unlike the ^{27}Al → ^{31}P 3Q-D-HETCOR spectrum described above, however, the relative intensity of the Al2−P2 cross peak is significantly weaker than those of the Al2−P1 or P2−Al1 cross peaks. It has been known from previous studies, that the $^2J_{AlP}$ coupling constant for the Al−O−P linkages (and more generally, $^2J_{TT'}$ for the T-O-T′ linkages, where T and T′ are tetrahedrally coordinated cations, such as P, Al, Si) is correlated with the Al−O−P angle, being smaller for smaller angles.[28,29] The weaker Al2−P2 cross peak suggests smaller Al2−O−P2 angles, compared to Al2−O−P1 and Al1−O−P2 angles. As will be discussed below, this is in agreement with the determined crystal structure.

Structure Analysis. Indexing of diffraction peaks by DICVOL[30] implemented in FOX resulted in a monoclinic cell. The lattice parameters of the phase are a = 8.7437(1) Å, b = 4.8584(1) Å, c = 10.8600(2) Å, β = 90.124(1)° (values after the Rietveld refinement). In order to achieve reasonable density, the number of formulas per unit cell (Z) must be 6. The density is then calculated as 2.634 g cm^{-3}, which is 0.5% higher than that of berlinite[31] under ambient conditions. The space group could not be uniquely determined at this stage, and thus all space groups that are consistent with the number and abundance ratio of P and Al sites determined from NMR and

dx.doi.org/10.1021/ic300167k | Inorg. Chem. 2012, 51, 6164−6172

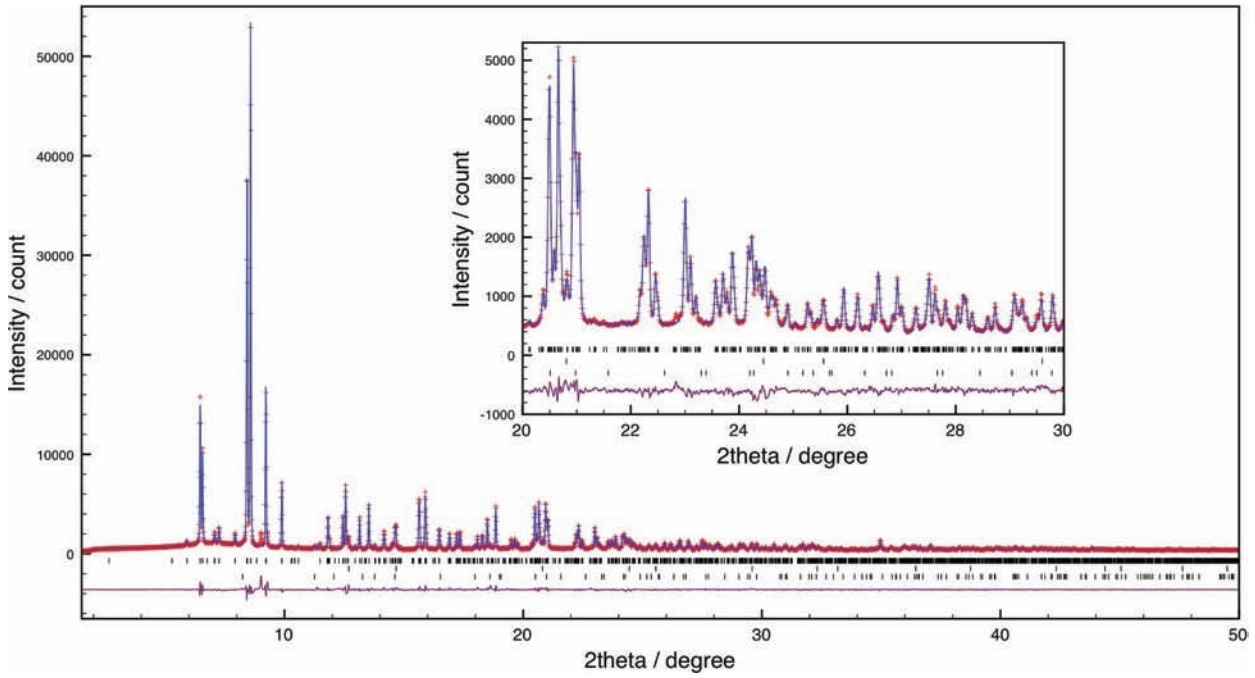

Figure 6. The Rietveld refinement pattern of moganite-$AlPO_4$. The observed intensities are shown by crosses, and the calculated intensities are shown by a line. The line at the bottom is the difference, and vertical ticks show positions of reflections. The ticks from top to bottom represent moganite phase, Pt, and corundum, respectively. Inset shows an enlarged pattern in the middle angle region.

give low R_{wp} by Le Bail profile fitting by FOX ($P2/m$, $P2/c$, $P2_1/c$, $P2_1/m$, $P2_1/n$) were tested in subsequent structural analysis. From the ^{31}P MAS and ^{27}Al 3Q MAS NMR study described above, two tetrahedral P and two tetrahedral Al sites each were identified. Accordingly, two independent PO_4 tetrahedra and two Al atoms were placed at general positions in the unit cell for FOX calculation. The structure with distinctly lower R_{wp} was obtained when the space group $P2/c$ (No. 13) was assumed. In order to facilitate structural comparison with moganite SiO_2 (reported as space group $I2/a$), $P2/a$, a nonstandard setting of $P2/c$, will be used in this paper. The structure obtained by FOX were then refined using the Rietveld method program RIETAN-FP.[24] The final R_{wp}, R_p, and S values for the pattern of the sample were 0.063, 0.040, and 1.81, respectively, and the R_B and R_F values of the $P2/a$ phase were 0.029 and 0.022, respectively. The fitted powder XRD pattern of the new $AlPO_4$ phase is shown in Figure 6, and the refined structural parameters are listed in Table 2. The same site names (e.g., P1, Al1) as described in the NMR section are adopted.

Structural Details. The refined crystal structure of the new $AlPO_4$ phase is shown in Figure 7. After refinement, it became clear that this phase is isostructural with moganite, which is one of the SiO_2 polymorphs. The occurrence of the moganite-type phase in $AlPO_4$ further confirms the close structural relationship between $AlPO_4$ and SiO_2. The structural features of moganite and its relationship with the structure of quartz have been described.[32] The moganite structure can be regarded as a periodic twinning of quartz according to the Brazil law on a unit-cell scale. The P2 and Al2 tetrahedra form a chain by sharing corners, running parallel to the b-axis. Four such chains are linked by P1 or Al1 tetrahedra to form a three-dimensional network structure (see Figure 7). One notable structural feature of the moganite phase is the existence of four-membered rings. Although four-membered rings are also present in coesite (a high-pressure SiO_2 phase), no such rings are known in other $AlPO_4$ polymorphs. Because of the ordered replacement of Al and P for Si sites in the moganite structure, the space group changed from $I2/a$ of moganite in SiO_2 to $P2/a$ of the $AlPO_4$ phase without doubling the cell like berlinite.

Table 2. Refined and DFT-Relaxed Structural Parameters of Moganite-$AlPO_4$ ($P2/a$, Space Group No. 13)[a]

a (Å)		b (Å)	c (Å)		β (°)
8.7437(1)		4.8584(1)	10.8600(2)		90.124(1)
(8.8865)		(4.9825)	(11.0183)		(90.36)
site	Wyckoff symbol	x	y	z	B_{iso}
P1	2e	1/4	0.9574(12)	0	0.39(2)
			(0.9698)		
P2	4g	0.5127(6)	0.2416(8)	0.6665(4)	0.39
		(0.5143)	(0.2514)	(0.6664)	
Al1	2f	1/4	0.4703(15)	1/2	0.39
			(0.4647)		
Al2	4g	0.5161(6)	0.2583(9)	0.1663(5)	0.39
		(0.5127)	(0.2438)	(0.1666)	
O1	4g	0.6865(8)	0.1557(15)	0.1002(7)	0.60(4)
		(0.6819)	(0.1505)	(0.0994)	
O2	4g	0.6254(7)	0.7888(12)	0.9453(7)	0.60
		(0.6290)	(0.7868)	(0.9428)	
O3	4g	0.5283(10)	0.9365(12)	0.7047(8)	0.60
		(0.5282)	(0.9577)	(0.7081)	
O4	4g	0.4740(11)	0.4080(11)	0.7840(7)	0.60
		(0.4773)	(0.4284)	(0.7780)	
O5	4g	0.6653(8)	0.3390(16)	0.6129(7)	0.60
		(0.6655)	(0.3365)	(0.6107)	
O6	4g	0.3864(8)	0.2490(14)	0.5671(7)	0.60
		(0.3870)	(0.2694)	(0.5709)	

[a]DFT results are shown in parentheses below the experimental values.

dx.doi.org/10.1021/ic300167k | Inorg. Chem. 2012, 51, 6164−6172

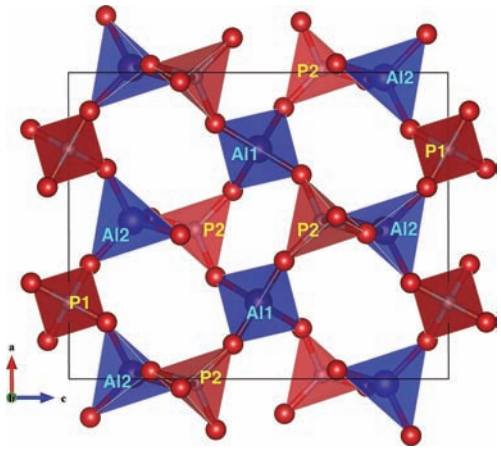

Figure 7. Projection of the crystal structure of moganite-$AlPO_4$ along the *b*-axis. Red tetrahedra represent PO_4, blue tetrahedra show AlO_4. Crystal structure is drawn by VESTA.[25]

The original moganite-SiO_2 has two independent Si sites with a 1:2 ratio. The $AlPO_4$ moganite phase inherits this and contains two sites for P and Al, each with a 1:2 ratio. This is fully consistent with the results by ^{31}P MAS NMR and ^{27}Al 3Q MAS NMR described above. In Table 2, the fractional coordinates of atoms in the $AlPO_4$ moganite phase are tabulated to be directly comparable with those of moganite-SiO_2.[33] Small positional displacements from the moganite-SiO_2 are noted. The corresponding parameters for the relaxed structure obtained from DFT calculation starting from the observed structure are also listed in Table 2. Slight changes in atomic positions and increase in cell parameters were observed during optimization. The latter is a well-known behavior when the GGA functional is used. The structure was stable even if symmetry constraints were removed during the relaxation calculation, confirming the stability of the phase. In the structure, each P1 (Al1) tetrahedron is bonded to four Al2 (P2) tetrahedra, and each P2 (Al2) tetrahedron is bonded to two Al1 (P1) tetrahedra and two Al2 (P2) tetrahedra. There are no Al1−O−P1 linkages. These are again fully consistent with the ^{27}Al−^{31}P 3Q-D-HETCOR and 3Q-J-HETCOR results described previously.

Selected bond distances and bond angles for the refined structure are listed in Table 3. These are generally similar to those of berlinite, but show more variations in the Al−O−P angles. As noted above, the ^{27}Al−^{31}P 3Q-J-HETCOR study suggests smaller P2−O−Al2 angles as compared to P1−O−Al2 and P2−O−Al1 angles. The determined crystal structure is completely consistent with the expected trend (with ∠P2−O−Al2 = 136.0°, 138.0°, ∠P2−O−Al1 = 141.8°, 145.1°, and ∠P1−O−Al2 = 141.0°, 150.2°). These results suggest that advanced solid-state NMR techniques are useful for revealing detailed local structural information for inorganic materials.

Table 3. Selected Bond Distances and Angles for the Refined Structure of Moganite-$AlPO_4$

bond distance		bond angle	
P1−O1 (×2)	1.486(7) Å	P1−O1−Al2	141.0(3)°
P1−O2 (×2)	1.557(8) Å	P1−O2−Al2	150.2(3)°
P2−O3	1.545(8) Å	P2−O3−Al2	136.0(4)°
P2−O4	1.549(8) Å	P2−O4−Al2	138.0(4)°
P2−O5	1.532(8) Å	P2−O5−Al1	145.1(3)°
P2−O6	1.543(8) Å	P2−O6−Al1	141.8(3)°
Al1−O5 (×2)	1.707(8) Å		
Al1−O6 (×2)	1.762(8) Å		
Al2−O1	1.729(9) Å		
Al2−O2	1.744(9) Å		
Al2−O3	1.736(9) Å		
Al2−O4	1.711(7) Å		

Stability of Moganite-Type Structure. This is the first moganite-type phase reported in the ABX_4 system (where A ≠ B). Although moganite is a rare phase, several related structures are known. For example, $Zn[BPO_4(OH)_2]$[34] has a moganite-like structure with an ordered distribution of three types of cations. BeH_2[35] has a structure closely related to moganite, whereas Na_2MnO_2[36] can be regarded as a stuffed moganite-type structure. Moganite-SiO_2 has been considered to be a metastable phase,[37] and no synthesis method is known to date. Only poorly crystallized natural samples intimately mixed with quartz are available, and have been used for previous structural studies. The existence of moganite-$AlPO_4$ was unexpected, because the moganite phase had never been regarded as a high-pressure form of quartz. For SiO_2, the reported density of moganite is 1.4% lower than that of quartz,[38] suggesting moganite as a low-density form of quartz. Moganite-type phase is also known for PON, which is another compound isoelectronic to SiO_2.[39] For PON, cristobalite phase is stable at ambient pressure, and a moganite-type phase (M) becomes stable between 1 and 3.5 GPa[40] The latter further transforms to quartz phase at higher pressure. Curiously, another moganite-type phase (M′) has also been observed at higher pressure on the higher-temperature side of the quartz stability field.[40] It was suggested that the M′ phase could possess a disordered orthorhombic structure under high pressure and temperature.[40] Recently, the crystal structure of δ-PON phase, which was synthesized in the stability region of M′ phase, was reported.[41] The structure is similar to moganite, but it has different topologies. No corresponding phase is observed in our study for $AlPO_4$. Thus, only the lower-pressure PON M phase will be compared. The phase transition between moganite and quartz phases in PON and $AlPO_4$ is in reverse order. The density of moganite-PON is 2.0% lower than that of quartz phase,[39] whereas the density of moganite is 0.5% higher than berlinite in $AlPO_4$ under ambient condition, as described above. The density contrast between the two phases is consistent with the observed phase relations (i.e., high-density phase being high-pressure phase). Compressibilities of moganite-PON and moganite-SiO_2 at room temperature have been reported to be larger than those of corresponding quartz phases.[40,42] Our preliminary first-principles calculation suggests a similar trend for $AlPO_4$. Thus, the moganite-$AlPO_4$ phase will be denser than berlinite at high pressure too. Structural similarity between moganite and quartz phases could be responsible for the change in their relative order of stability, depending on chemical composition.

Structural stability of the ABX_4 system has been discussed using plots of the ionic radius ratios of the constituent ions in the compounds.[2,3] Errandonea and Manjón[43] presented an updated version of such plot (r_A/r_X vs r_B/r_X) for the structure fields of many ABX_4 compounds. Figure 8 shows an enlarged part of the plot near SiO_2 and $AlPO_4$ after Errandonea and Manjón with some modifications. The regions for cristobalite, quartz, and *Cmcm* phases ($CrVO_4$ or $InPO_4$) are shown according to each compound's stable structure at ambient pressure. The $AlVO_4$ stability field is added here. In the original

dx.doi.org/10.1021/ic300167k | Inorg. Chem. 2012, 51, 6164−6172

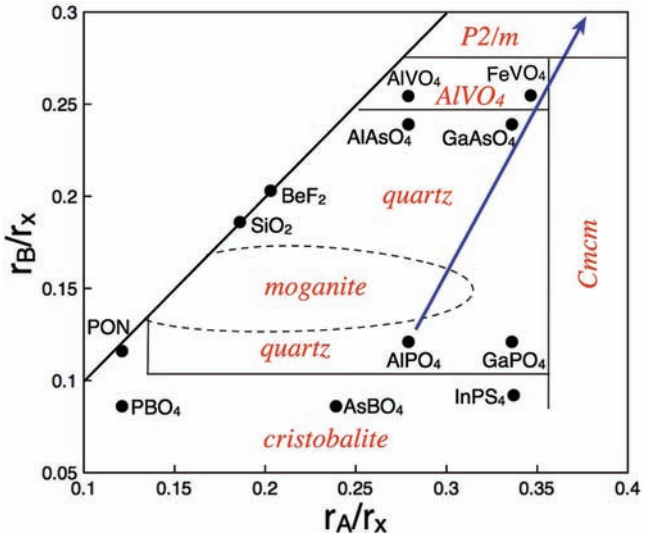

Figure 8. Ionic radius ratio (r_A/r_X vs r_B/r_X) plot of structure fields for the ABX_4 system, modified after Errandonea and Manjón.[43] For PON, r_P/r_N vs r_P/r_O is plotted. Stability fields of cristobalite, quartz, $AlVO_4$, *P*2/*m*, and *Cmcm* phases are shown. Hypothetical stability field for moganite is also shown by the broken line. An arrow indicates a possible pressure-induced structural transition sequence for $AlPO_4$.

plot,[43] $AlVO_4$ and $FeVO_4$ are placed in the region where all cations are in octahedral sites. However, this is not correct, and Al or Fe are in both five- and six-coordination sites. The finding of the $AlVO_4$-type $AlPO_4$ phase by us further supports this stability region. The compounds with moganite structure observed so far are located in the left-lower corner of the quartz field (r_A/r_X = 0.12−0.28; r_B/r_X = 0.12−0.18). This suggests that the moganite phase will be favored at relatively smaller r_A and r_B values, compared to the wide quartz field. Although no stable moganite phase at ambient pressure is known to date, a hypothetical moganite field may be drawn on the plot, considering the phase relations and density contrasts between quartz and moganite in PON, SiO_2, and $AlPO_4$. The plot can be used to explain pressure-induced phase transition sequences. Because of greater compressibility for the larger anion, higher-pressure phases are expected in the increasing r_A/r_X and increasing r_B/r_X direction of the plot.[43] The quartz phase of $AlPO_4$ transforms to the moganite phase (assuming the present hypothetical field), and then further transforms to $AlVO_4$ and/or *Cmcm* phases at higher pressures, as shown by the arrow in Figure 8. This is as observed in our study,[4] except for a missing field for the observed $P2_1/c$ phase. BeF_2 has been regarded as a closest analogue of SiO_2 from the plot, and even the rare coesite phase is known for BeF_2.[3] However, no moganite phase has been observed so far. This can be explained by the higher r_A/r_X and r_B/r_X for BeF_2 than SiO_2. This plot also implies that PBO_4 and $AsBO_4$ cristobalite phases could transform to quartz and/or moganite phases under pressure. Indeed, these compounds have been reported to transform to quartz phase at high pressure.[3] Although no moganite phase has been reported to date, it could be expected at even higher pressure.

Similar to quartz and cristobalite, moganite-SiO_2 undergoes temperature-induced displacive phase transition at 570 K, transforming from monoclinic (*I*2/*a*) to orthorhombic cell (*Imab*).[33,37] Similar displacive transition is well-known for berlinite and, thus, may occur for the moganite-type $AlPO_4$ phase as well. In this respect, the phase observed in the present study should be referred to as low-temperature or α-moganite phase. Our preliminary first-principles calculation suggests that the high-temperature form would adapt space group *Pmaa* (No. 49). Unlike SiO_2, a well-crystallized sample can be readily obtained for $AlPO_4$, rendering it an ideal system for structural studies of the moganite-type phase.

In summary, we have found a new high-pressure phase of $AlPO_4$ phase at 5 GPa and 1500 °C, and we have determined its structure from NMR and synchrotron powder X-ray diffraction. Detailed NMR study revealed the number of P and Al sites, their oxygen coordination numbers, abundance ratios and linkages. These data helped to solve the crystal structure using powder X-ray diffraction data. NMR parameters of the phase were also calculated by first-principles technique using the crystal structure obtained after relaxation, which are consistent with those observed. This phase is isostructural to moganite SiO_2, and is the first such phase found in the ABX_4 system (A ≠ B). The existence of moganite phase in $AlPO_4$ further emphasizes the close structural similarity between SiO_2 and $AlPO_4$. Unlike SiO_2 and PON, moganite-type $AlPO_4$ is a stable higher-pressure phase of berlinite (quartz phase). Other moganite phases in the ABX_4 system might be expected and warrant further investigation.

■ ASSOCIATED CONTENT

Ⓢ Supporting Information

Crystallographic data for moganite-$AlPO_4$ phase in CIF format. This material is available free of charge via the Internet at http://pubs.acs.org.

■ AUTHOR INFORMATION

Corresponding Author

*E-mail: mkanzaki@misasa.okayama-u.ac.jp.

Notes

The authors declare no competing financial interest.

■ ACKNOWLEDGMENTS

We would like to thank two anonymous reviewers for helpful comments and suggestions. We also thank Dr. Ken-ichi Funakoshi for permission to use of the SPEED1500 press at SPring-8. Synchrotron powder X-ray diffraction pattern was measured at BL19B2 of SPring-8 (Proposal No. 2011B1990). This study was supported by Grants-in-Aid for Scientific Research funded by the Ministry of Education, Culture, Sports, Science and Technology of Japan.

■ REFERENCES

(1) Flörke, O. *Z. Kristallogr.* **1967**, *Bd.125*, S134−146.
(2) Seifert, K.-F. *Fortschr. Miner.* **1968**, *45*, 214−280.
(3) Dachille, F.; Roy, R. *Z. Kristallogr.* **1959**, *111*, S.451−461.
(4) Kanzaki, M.; Xue, X.; Reibstein, S.; Berryman, E.; Namgung, S. *Acta Crystallogr., Sect. B: Struct. Sci.* **2011**, *67*, 30−40.
(5) Pellicer-Porres, J.; Saitta, A. M.; Polian, A.; Itié, J. P.; Hanfland, M. *Nat. Mater.* **2007**, *6*, 698−702.
(6) Heaney, P. J.; Post, J. E. *Science* **1992**, *255*, 441−443.
(7) van Beek, J. *J. Magn. Reson.* **2007**, *187*, 19−26.
(8) Hohwy, M.; Jakobsen, H.; Eden, M.; Levitt, M.; Nielsen, N. *J. Chem. Phys.* **1998**, *108*, 2686−2694.
(9) Amoureux, J.-P.; Fernandez, C.; Steuernagel, S. *J. Magn. Reson. A* **1996**, *123*, 116−118.
(10) Amoureux, J.-P.; Fernandez, C. *Solid State Nucl. Magn. Reson.* **1998**, *10*, 211−223.

(11) Wiench, J. W.; Tricot, G.; Delevoye, L.; Trebosc, J.; Frey, J.; Montagne, L.; Amoureux, J.-P.; Pruski, M. *Phys. Chem. Chem. Phys.* **2006**, *8*, 144−150.
(12) Yates, J.; Pickard, C.; Mauri, F. *Phys. Rev. B* **2007**, *76*, 024401.
(13) Giannozzi, P.; et al. *J. Phys: Condens. Matter* **2009**, *21*, 395502.
(14) Perdew, J.; Burke, K.; Ernzerhof, M. *Phys. Rev. Lett.* **1996**, *77*, 3865−3868.
(15) Pickard, C. J.; Mauri, F. *Phys. Rev. B* **2001**, *63*, 245101.
(16) Troullier, N.; Martins, J. *Phys. Rev. B* **1991**, *43*, 8861−8869.
(17) Xue, X. *Solid State Nucl. Magn. Reson.* **2010**, *38*, 62−73.
(18) Huguenard, C.; Taulelle, F.; Knott, B.; Gan, Z. *J. Magn. Reson.* **2002**, *156*, 131−137.
(19) Pyykkö, P. *Mol. Phys.* **2008**, *106*, 1965−1974.
(20) Ashbrook, S. E.; Cutajar, M.; Pickard, C. J.; Walton, R. I.; Wimperis, S. *Phys. Chem. Chem. Phys.* **2008**, *10*, 5754−5764.
(21) Byrne, P.; Warren, J.; Morris, R.; Ashbrook, S. E. *Solid State Sci.* **2009**, *11*, 1001−1006.
(22) Nishibori, E.; Takata, M.; Kato, K.; Sakata, M.; Kubota, Y.; Aoyagi, S.; Kuroiwa, Y.; Yamakata, M.; Ikeda, N. *Nucl. Instrum. Methods Phys. Res. A* **2001**, *467−468*, 1045−1048.
(23) Favre-Nicolin, V.; Cérný, R. *J. Appl. Crystallogr.* **2002**, *35*, 734−743.
(24) Izumi, F.; Momma, K. *Solid State Phenom.* **2007**, *130*, 15−20.
(25) Momma, K.; Izumi, F. *J. Appl. Crystallogr.* **2011**, *44*, 1272−1276.
(26) MacKenzie, K. J. D.; Smith, M. In *Multinuclear Solid-State NMR of Inorganic Materials*; Cahn, R., Ed.; Pergamon Materials Series; Pergamon: Amsterdam, 2002; Vol. *6*; p 727.
(27) Amoureux, J.-P.; Fernandez, C.; Frydman, L. *Chem. Phys. Lett.* **1996**, *259*, 347−355.
(28) Cadars, S.; Brouwer, D. H.; Chmelka, B. *Phys. Chem. Chem. Phys.* **2009**, *11*, 1825−1837.
(29) Massiot, D.; Fayon, F.; Alonso, B.; Trebosc, J.; Amoureux, J.-P. *J. Magn. Reson.* **2003**, *164*, 160−164.
(30) Boultif, A.; Louer, D. *J. Appl. Crystallogr.* **1991**, *24*, 987−993.
(31) Muraoka, Y.; Kihara, K. *Phys. Chem. Mineral.* **1997**, *24*, 243−253.
(32) Miehe, G.; Graetsch, H. *Eur. J. Mineral.* **1992**, *4*, 693−706.
(33) Heaney, P. J.; Post, J. E. *Am. Mineral.* **2001**, *86*, 1358−1366.
(34) Huang, Y.-X.; Prots, Y.; Kniep, R. *Chem.—Eur. J.* **2008**, *14*, 1757−1761.
(35) Smith, G.; Johnson, Q.; Smith, D.; Cox, D.; Snyder, R.; Zhou, R.-S. *Solid State Commun.* **1988**, *67*, 491−494.
(36) Pfeiffer, S.; Jansen, M. *Z. Anorg. Allg. Chem.* **2009**, *635*, 211−215.
(37) Heaney, P. J.; McKeown, D. A.; Post, J. E. *Am. Mineral.* **2007**, *92*, 631−639.
(38) Navrotsky, A.; Petrovic, I.; Hu, Y.; Chen, C.-Y.; Davis, M. *Microporous Mater.* **1995**, *4*, 95−98.
(39) Chateau, C.; Haines, J.; Léger, J. M.; LeSauze, A.; Marchand, R. *Am. Mineral.* **1999**, *84*, 207−210.
(40) Léger, J. M.; Haines, J.; Chateau, C.; Bocquillon, G.; Schmidt, M.; Hull, S.; Gorelli, F.; Lesauze, A.; Marchand, R. *Phys. Chem. Mineral.* **2001**, *28*, 388−398.
(41) Baumann, D.; Sedlmaier, S.; Schnick, W. *Angew. Chem.* **2012**, *124*, 1−4.
(42) Léger, J. M.; Haines, J.; Chateau, C. *Eur. J. Mineral.* **2001**, *13*, 351−359.
(43) Errandonea, D.; Manjón, F. *Prog. Mater. Sci.* **2008**, *53*, 711−773.